Journal of Biomedical Optics

SPIEDigitalLibrary.org/jbo

Phasor imaging with a widefield photon-counting detector

Ryan A. Colyer
Oswald H. W. Siegmund
Anton S. Tremsin
John V. Vallerga
Shimon Weiss
Xavier Michalet

SPIE

Phasor imaging with a widefield photon-counting detector

Ryan A. Colyer,[a] Oswald H. W. Siegmund,[b] Anton S. Tremsin,[b] John V. Vallerga,[b] Shimon Weiss,[a] and Xavier Michalet[a]
[a]UCLA, Department of Chemistry and Biochemistry, 607 Charles E. Young Drive East, Los Angeles, California
[b]Space Sciences Laboratory, UCB, 7 Gauss Way, Berkeley, California

Abstract. Fluorescence lifetime can be used as a contrast mechanism to distinguish fluorophores for localization or tracking, for studying molecular interactions, binding, assembly, and aggregation, or for observing conformational changes via Förster resonance energy transfer (FRET) between donor and acceptor molecules. Fluorescence lifetime imaging microscopy (FLIM) is thus a powerful technique but its widespread use has been hampered by demanding hardware and software requirements. FLIM data is often analyzed in terms of multicomponent fluorescence lifetime decays, which requires large signals for a good signal-to-noise ratio. This confines the approach to very low frame rates and limits the number of frames which can be acquired before bleaching the sample. Recently, a computationally efficient and intuitive graphical representation, the phasor approach, has been proposed as an alternative method for FLIM data analysis at the ensemble and single-molecule level. In this article, we illustrate the advantages of combining phasor analysis with a widefield time-resolved single photon-counting detector (the H33D detector) for FLIM applications. In particular we show that phasor analysis allows real-time subsecond identification of species by their lifetimes and rapid representation of their spatial distribution, thanks to the parallel acquisition of FLIM information over a wide field of view by the H33D detector. We also discuss possible improvements of the H33D detector's performance made possible by the simplicity of phasor analysis and its relaxed timing accuracy requirements compared to standard time-correlated single-photon counting (TCSPC) methods. [DOI: 10.1117/1.JBO.17.1.016008]

Keyword: detectors; fluorescence; imaging; laser-induced fluorescence; microscopy.

Paper 11383P received Jul. 19, 2011; revised manuscript received Nov. 6, 2011; accepted for publication Nov. 15, 2011; published online Feb. 7, 2012.

1 Introduction

1.1 *FLIM Overview*

In biology, fluorescence microscopy is a powerful tool for imaging fixed samples, live cells, or even live animals due to its sensitivity, specificity, versatility, and noninvasiveness.[1] In addition to providing an array of probes allowing different molecular species to be detected in different color channels, fluorescence microscopy can be combined with polarization-sensitive or time-resolved detection to enhance its sensitivity and provide additional information on molecular dynamics and the chemical environment. Fluorescence lifetime imaging microscopy (FLIM), which is based on the measurement of the fluorescence emission decay time after excitation, has gained popularity due to several advantages over intensity-only measurements.[2–8] For instance, FLIM information allows separating signal coming from an uncorrelated background from the signal of interest. Moreover, when background autofluorescence is characterized by a different lifetime than the signal of interest, FLIM provides a simple way of distinguishing both signals.[9,10] Since fluorescence lifetime is unaffected by a large range of concentrations, this information can be extracted independently from signal intensity; the latter being concentration-dependent. In general, this added dimension makes FLIM analysis more powerful than intensity-based or even ratiometric intensity methods for separating concentration and background effects from those attributable to the signal of interest.[11] More importantly, some probes have a fluorescence lifetime which is sensitive to the local chemical environment such as ion concentration[12–15] or pH.[11,16] A powerful use of FLIM is in Förster resonance energy transfer (FRET) studies, in which a donor molecule nonradiatively transfers its excitation energy to a nearby acceptor fluorophore. The donor lifetime is reduced due to energy transfer and its measurement directly reports on the distance between the two fluorophores, making it a technique of choice for conformational changes or molecular interaction studies down to the single-molecule level.[17]

1.2 *FLIM Data Acquisition*

Despite these numerous theoretical advantages, FLIM still requires sophisticated equipment and approaches to analysis that have limited its widespread use. We will briefly review these two aspects and argue that the combination of a new detector technology and phasor analysis provides an attractive enhancement. FLIM microscopy can be implemented using either confocal or widefield geometries. Standard confocal raster-scanning systems can be simply upgraded to acquire FLIM images by adding a pulsed or modulated laser source and additional signal processing electronics. Some systems may require detectors with faster response. Confocal FLIM using frequency-modulated photomultiplier tubes (PMT) has been successfully

Address all correspondence to: Ryan Colyer, UCLA, Department of Chemistry and Biochemistry, 607 Charles E. Young Drive East, Los Angeles, California. Tel: 3107946693; E-mail: ryancolyer@yahoo.com and Xavier Michalet, UCLA, Department of Chemistry and Biochemistry, 607 Charles E. Young Drive East, Los Angeles, California; E-mail: michalet@chem.ucla.edu.

0091-3286/2012/$25.00 © 2012 SPIE

demonstrated,[18] but with substantial loss in photon collection efficiency.[19,20] Instead, most confocal FLIM systems use PMTs or single-photon avalanche photodiodes (SPAD) with time-correlated single-photon counting[21] or digital frequency domain (DFD)[20] hardware. As in standard confocal imaging, confocal FLIM systems are in principle capable of video frame rates (~30 Hz) or faster.[22] However, since the dwell-time per pixel is short, good signal-to-noise ratio (SNR) requires extremely high count rates, which excludes faint samples and results in accelerated sample photobleaching and phototoxicity. For example, a 256×256 pixel image refreshed at 30 frames per second requires a dwell time of only half a microsecond per pixel. Therefore, to obtain even only a few tens of photons per pixel of interest, count rates of many tens of millions of counts per second (cps) are needed. In addition to being demanding on the sample, these count rates exceed the capabilities of typical point detectors such as PMTs and SPADs[19] and are also beyond the processing capabilities of current TCSPC electronics. In practice, lower count rates are collected (below 1 MHz) and since large counts per pixels are needed for proper FLIM analysis, frame rates much lower than 1 Hz are typical of confocal FLIM.

Widefield FLIM is usually performed using time-gated[23–25] or frequency modulated[4,26] image intensifiers, which are lens- or fiber-coupled to charge-coupled device (CCD) or complementary metal-oxide semiconductor (CMOS) cameras. Z-sectioning capability comparable to that of laser scanning confocal microscopes is now possible using spinning disk systems,[26–28] although that requires significantly higher laser powers. Whereas data is acquired in parallel in each pixel of the image, allowing in principle fast frame rates, these detectors do not have single-photon counting capability and have significant readout noise, making them inefficient for low-light level imaging. Additionally, the intensification mechanism results in reduced dynamic range preventing very bright samples or samples with large dynamic range to be studied as well. In the case of time-gating, a significant fraction of collected photons are rejected, adding to the inefficiency of the technique.[20]

These fundamental hardware constraints may explain in part the limited success of FLIM. In particular, it remains a challenge to obtain rich lifetime information over many pixels rapidly and in an easily interpretable manner.

1.3 *FLIM Data Analysis*

The issue of data interpretation is often overlooked when discussing FLIM, but may be another fundamental reason for the limited adoption of the technique. The usual way to analyze fluorescence decay data is to interpret it as the sum of independent lifetime components with each component being modeled by a single exponential decay. There are a number of issues with this assumption, both from a theoretical and from a practical point of view. From a theoretical point of view, the underlying hypothesis is that the sample or molecules within a pixel of the image is comprised of only a few species, each characterized by a single, well-defined lifetime. This assumption is sometimes replaced by the slightly more flexible model of a continuous distribution of species with unique lifetimes or by a "stretched" exponential.[29] The question is whether or not to let each component vary from one pixel to the next, or constrain them to correspond to a few independently measured lifetimes, and in general, how to interpret the numerical results microscopically.

From a practical point of view, none of these models is easy to verify experimentally. Even in the case of a few species, there are well-known numerical issues with trying to fit a photon-limited decay histogram with more than a few single-exponential components.[30] Last, representing the many parameters resulting from this analysis (individual lifetimes and the amplitudes of each component) is cumbersome and requires juggling many color maps representing complex ratios or condensed information in a nonintuitive manner.

1.4 *New Approach to FLIM*

To make FLIM more accessible and attractive, hardware and software limitations need to be addressed simultaneously. We will first describe the advantages of a new widefield photon-counting device for imaging under low-light conditions. Next, we will discuss the merits of phasor analysis. Finally, we will show how both complement each other to provide a platform for a simple yet powerful implementation of FLIM.

1.4.1 *Widefield photon-counting detector*

To compare widefield and raster-scanning FLIM and understand when the widefield approach becomes advantageous, it is useful to estimate the time needed to acquire the same information in the two approaches. Using Fig. 1 to illustrate, we examine how to use both methods to obtain the same number of photons n_{ij} in each pixel (i,j) of an $N \times N$ pixel image (in order to obtain the same SNR). Defining $r(i,j)$ as the local incident photon rate at pixel (i,j), Δt as the dwell time per pixel, QE as the quantum efficiency, and indicating raster scanning by subscript p and widefield by subscript w, the number of photons for each pixel is given by:

$$n_{ij} = r_p(i,j)\Delta t_p QE_p = r_w(i,j)\Delta t_w QE_w. \quad (1)$$

For a raster-scanning approach using a point detector, the total acquisition time for an image is proportional to the number of pixels $(N \times N)$ in the image: $T_p = N^2 \Delta t_p$ and the global detected count rate for the whole image is $G_p = \langle r_p \rangle QE_p$, where $\langle r_p \rangle$ is the average local incident photon rate in the image. In other words, in a raster-scanning approach, the global detected count rate is equal to the average detected local count rate.

In a widefield approach, the dwell time is by definition equal to the frame duration ($T_w = \Delta t_w$). Since counts are collected across the entire frame in parallel, the widefield global detected count rate is then

$$G_w = N^2 \langle r_w \rangle QE_w. \quad (2)$$

To compare the two acquisition rates fairly, we need to consider the best scenarios for each method. In a raster-scanning approach, the main limit is typically the maximum sustainable incident photon rate, $r_p^{\max}$, which is usually on the order of a few 100 kHz due to sample limitations.[31] In a widefield photon counting approach, the main limit is generally the sustainable global count rate of the electronics, $G_w^{\max} < 100$ MHz.[32–34]

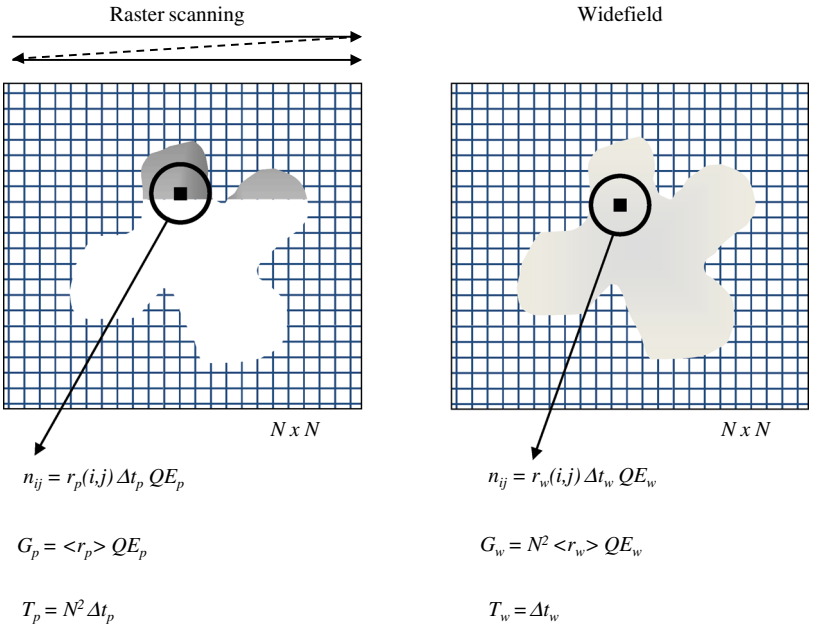

Fig. 1 Comparison between raster-scanning and widefield single-photon counting FLIM approaches. An identical $N \times N$ pixel image is acquired by the two types of detector (point-detector –P and widefield detector –W). The dwell time per pixel $\Delta t_{P,W}$ is adjusted so that, despite the different quantum efficiencies $QE_{P,W}$, for a given incident photon rate $r(i, j)$ both detectors collect the same number of photons n_{ij}. The global count rates $G_{P,W}$ and total frame duration $T_{P,W}$ are indicated. A widefield approach requires in general a much shorter integration time but results in much larger global count rate than a raster-scanning approach using a point detector.

To compare the local limit $r_p^{\max}$ of the raster scanning approach with the global limit $G_w^{\max}$of the widefield approach in the most general case, it is necessary to introduce an image profile factor, f:

$$f = \frac{\langle n_{ij} \rangle}{n^{\max}} = \frac{\langle r_{ij} \rangle}{r^{\max}}, \tag{3}$$

characterizing the signal uniformity in the image. For a uniform image, $f = 1$, while for sparsely labeled images, $f \ll 1$. A typical cell image, like the schematic in Fig. 1, will have an intermediate value in the interval [0, 1]. By constraining for the same number of detected photons in each pixel, we obtain the following expression for the ratio between the raster scanning and widefield image acquisition times:

$$T_p/T_w = \frac{G_w^{\max}}{f r_p^{\max} QE_p}, \tag{4}$$

where f and $r_p^{\max}$ are properties of the sample, and $G_w^{\max}$ and QE_p are properties of the detectors. Eq. (4) expresses the fact that a widefield approach is faster than a raster-scanning approach if the former can sustain a global detected count rate ($G_w^{\max}$) which is larger than the maximum local detected count rate ($r_{\max} QE_p$) of the point detector. It also expresses the fact that the speed gain in favor of the widefield approach is largest for sparsely labeled images ($f \ll 1$). In theory, gains of several orders of magnitude can be obtained.

Note also that under the condition of this comparison (equal photon counts in both images), the ratio between the local count rates is:

$$\frac{r_w}{r_p} = \frac{G_w^{\max}}{N^2 \langle r_p \rangle QE_w}. \tag{5}$$

Because the number of pixels N^2 is very large, e.g. 512×512, and the term $\langle r_p \rangle QE_w$ is on the order of tens of kHz, while $G_w^{\max}$ is constrained to less than 100 MHz, this makes the widefield photon rate r_w much smaller than the local photon rate r_p by a factor of more than 10. This shows that a lower sample excitation rate is needed for a widefield detector, which protects the sample from photobleaching and phototoxicity.

It should be noted that regulations of clinical use of laser light consider the total excitation light transmitted to the patient, and raster scanning makes better use of the total light available. Therefore, regulations for maximum permissible exposure limits may allow higher count rates with raster scanning FLIM in clinical applications.[35]

In the rarer case where the sample is not bright enough to reach the global count rate limit of the detector $G_w^{\max}$ such as for a very sparse sample as with single particle tracking, Eq. (4) can be rewritten as:

$$T_p/T_w = \frac{N^2 \langle r_w \rangle QE_w}{\langle r_p \rangle QE_p}. \tag{6}$$

With no limitation here of the global count rate the advantages of the widefield approach are even more pronounced, as the acquisition is performed approximately N^2 faster.

Even though we have limited this discussion to photon-counting detectors, it is also possible to treat other approaches (e.g. time-gated cameras). For example, modulated or gated cameras have the advantages of widefield acquisition, however, they discard photons during their "off" states and a corresponding reduction in achievable frame rate occurs. A complete discussion including the effects of camera noise on FLIM precision is beyond the scope of this paper.

One of the main advantages of a widefield photon-counting device over either a raster-scanning photon-counting approach or an integrating widefield detector is the possibility to arbitrarily define the start and end times of a frame. As discussed previously, it is possible to adjust the frame duration (online or post-acquisition) in order to achieve a target SNR. This is not possible in other approaches, in which the acquisition sequence (dwell time and number of scanning steps for a raster-scanning approach or number of time gates in a time-gated widefield approach) need to be defined beforehand.

Although widefield photon-counting detectors capable of accurate photon timing and good spatial resolution have been available for many decades, they had low maximum global count rates (<100 kHz), poor quantum efficiency, and in general limited availability and high cost.[36–42] To circumvent these limitations, we have started the development of a new widefield photon-counting detector called the H33D*, the first prototype of which has been described in a series of recent papers.[32,33,43–46] Our goal is to develop a detector with a spatial resolution comparable to a standard camera (512×512 pixels), a temporal resolution allowing the measurement of fluorescence lifetimes encountered in typical FLIM applications (>100 ps), a quantum efficiency comparable to that of the best PMTs ($QE \sim 40$ 50% in the visible spectrum), a maximum local count rate of ~100 kHz and a maximum global count rate of ~10 MHz.

Our first prototype, the Gen I H33D detector described in Sec. 2.3, meets these specifications as far as spatial and temporal resolutions are concerned, but has a modest $QE < 10\%$ in the visible range, a maximum local count rate of ~10 kHz and a maximum global count rate of ~500 kHz. Despite its low QE, the Gen I H33D detector has a maximum global count rate several times larger than the typical average count rate in a raster-scanning FLIM image, resulting in a potentially faster FLIM frame rate than raster-scanning FLIM.

1.4.2 *Phasor analysis*

In all of the photon-counting approaches lifetime data is acquired as a histogram of time-resolved values, which for typical fluorophores requires time resolution of a few nanoseconds or better.[20,47] For a conventional time-domain analysis, this data is then fit to one or more exponentials or stretched exponentials[29,48] convolved with an instrument response function (IRF) which represents both the temporal profile of the excitation light and the time response of the measurement device.[49,50] In an ideal case with no background, a zero-width IRF (delta function) and a single exponential decay, ~185 photons are required to obtain a lifetime uncertainty of around 10% using either least-square fitting or maximum likelihood methods.[47,51] If the sample contains two exponential decay components, the same analysis would require on the order of hundreds of thousands of photons to obtain the same lifetime uncertainty for both components,[47] which for raster-scanning with a 256×256 FLIM image requires acquisition times on the order of hours.[52] Photobleaching and phototoxicity introduce practical constraints on the total acquisition time and thus the total number of photons that can be collected,[53] therefore limiting the potential usefulness of multicomponent FLIM analysis for live-cell imaging.[52]

Fast algorithms have been developed for initial parameter estimation[54] and for global fitting of FLIM images with calculation times per frame ranging from minutes to hours, but for biexponential samples this still requires thousands of counts per pixel per frame, and the run time is highly sensitive to the initial parameter guesses.[50] Under the count constraints imposed by photobleaching, there are no fitting methods for FLIM images which can reliably extract three or more nanosecond scale exponentials, as this only works with well separated lifetimes ($\tau_{i+1}/\tau_i > 5$) and would require on the order of millions of counts per pixel.[55,56] Additionally, it is often impossible to know how many exponential components are present in an image, and it is often not possible to make an unambiguous interpretation of multiexponential images.[57] These difficulties with fitting and interpretation of FLIM image data have motivated the recent developments of phasor analysis, a fit-free analysis method for lifetime data.

Phasor analysis was first developed for frequency-domain analysis of lifetimes in phase and modulation fluorometry. The angle given by phase and the magnitude given by modulation, were used to form vectors called phasors which were used to examine the properties of single exponential and multiexponential lifetimes.[58] The frequency domain equations were then adapted to images to facilitate global fitting of FLIM data.[59] More recently, these equations were extended to the analysis of lifetime images by producing a graphical histogram of the phase and modulation values at each pixel of an image, allowing the rapid examination of lifetime distributions, the calculation of population ratios, and quantitative FRET analysis.[60–65]

The calculation of phasors is extremely rapid, as the phasor coordinate for every pixel is obtained by a simple algebraic operation on the photon arrival times collected in that pixel.[61] Phasor analysis also requires no initial guesses about the data and handles multicomponent decays (such as commonly found in a cell) seamlessly.[62] These capabilities make phasor analysis an ideal approach for a widefield photon-counting detector, as they allow a continuous update of FLIM information at each pixel. For example, this permits the continuous update of a map which shows the relative amounts of two different molecular species as described in Sec. 3.1.

Combined with the capability of a widefield photon-counting detector to arbitrarily define the start and end time of a frame, phasor analysis allows obtaining the most efficient balance between fast frame rate and good SNR by adjusting the duration of each frame, either online or postacquisition, and then binning the phasors accordingly (see Sec. 2.4) This is in contrast with the way phasor data is computed in other methods: in raster-scanning FLIM using TCSPC or DFD, lifetime information is typically binned into a histogram for each pixel in a frame, and the phasor coordinates are then calculated algebraically from this histogram, producing a phasor plot corresponding to that frame. In widefield FLIM with intensified CCDs, photons are acquired for various time bins (time-gated acquisition) or phase offsets (frequency-modulated acquisition), similarly producing a histogram of intensities for each frame, and phasor coordinates are then calculated for each pixel.

*pronounced "heed" for High spatial, High temporal resolution, High throughput 3D detector, where the three dimensions correspond to two spatial and one temporal dimension.

2 Materials and Methods

2.1 *Sample*

Cells. The sample preparation was previously described in Ref. 43. Briefly, quantum dots (QDs) emitting at 620 nm and coated with nonbiotinylated peptides were targeted to HeLa cells that stably express a glycosylphosphatidylinositol (GPI)-anchored avidin (GPI-av)[66,67] and caveolin 1-EGFP (Cav1-EGFP). For imaging, HeLa cells were grown in Dulbecco's modified Eagle medium (DMEM) media supplemented with 5% fetal calf serum on fibronectin-coated temperature-regulated wells (SmartSlide 100, Wavergen, Fremont, CA). Cells were kept at 37 °C through all labeling steps and during imaging. Cells were preincubated in a HBSS + 1% BSA buffer for 10 min before the addition of 10 nM QDs. QDs were incubated overnight with HeLa cells, resulting in nonspecific endocytosis. Cells were then rinsed with DMEM medium and imaged at 37 °C.

Beads. 220 nm diameter Nile Red fluorescent beads (Invitrogen) (excitation peak: 535 nm/emission peak: 575 nm) were diluted 100 times in Tris-EDTA buffer, sonicated for 5 min and centrifugated at 14 000 rcf (relative centrifugal force). 10 μL of the supernatant were spin coated on cleaned glass coverslip (4000 rpm) before observation.

Single quantum dots: 5 mg of 577 nm emitting CdSe/ZnS core shell quantum dot powder (Ocean Nanotech, Springdale, AR) were diluted in 1 mL butanol. After 2 successive 100 times dilutions in butanol, 10 μL of the sample were spin coated on a cleaned glass coverslip (4000 rpm) before observation.

2.2 *Experimental Setup*

The experimental setup used in these experiments is shown in Fig. 2, and is similar to the setup in.[33] Briefly, the sample was excited using either of the two following laser sources. For live-cell imaging, the output of a 76 MHz pulsed femtosecond Ti:Sa laser (Mira 900, Coherent, Santa Clara, CA) pumped by an Argon ion laser (Sabre, Coherent) was decimated down to a 4.75-MHz repetition rate using a pulse-picker (Model 9200, Coherent) and frequency-doubled using a BBO crystal (Casix, Mountain Lakes, NJ). The resulting 442 nm pulsed light was expanded and focused on the back focal plane of a high numerical aperture (NA = 1.45, magnification: 60×) objective lens of an inverted widefield microscope (IX 71, Olympus, Center Valley, PA) to obtain epifluorescence illumination of the sample. For single quantum dot and bead imaging, a pulsed picosecond 532-nm laser (IC-532-1000, High Q Laser, Watertown, MA) was coupled to a single-mode fiber and injected into the total internal reflection (TIR) illumination port of the microscope.

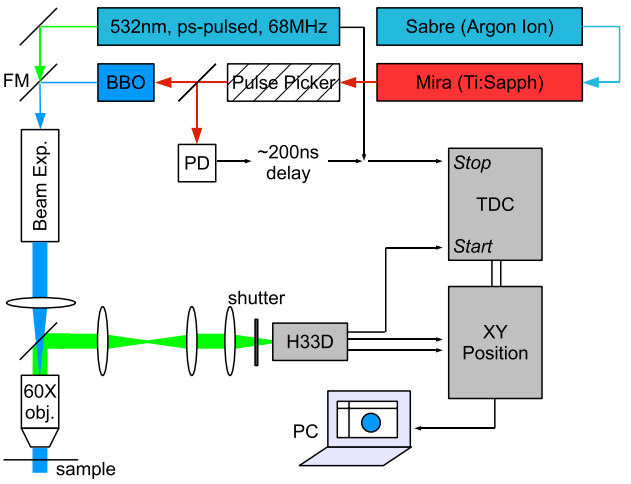

Fig. 2 The experimental setup is shown. Two lasers were used, selected by a flippable mirror. For one, a 76 MHz Ti:Sapph was pulse-picked down to 4.75 MHz, then frequency-doubled to 460 nm, while for the other, a 532 nm 68 MHz laser with pulses 8 ps wide was used. Both lasers were then expanded and focused in the back focal plane of the objective to produce widefield illumination. The emitted light was collected by relay optics and imaged onto the H33D. Timing information from the H33D was used to calculate lifetime information relative to a photodiode pulse measured from the excitation lasers.

In both cases, widefield fluorescence emission was collected using appropriate dichroic mirrors and emission filters, and imaged onto the H33D detector using relay optics resulting in a total magnification of 125×.

2.3 *The H33D Detector*

The H33D detector is a time-resolved widefield single-photon counting device, which we have previously described.[10,32,33,44,45,68] Briefly, each detected photon is first converted into a photoelectron by a photocathode deposited on the internal face of the input window. The photoelectron is then accelerated by a high-voltage difference and penetrates into a microchannel of a microchannel plate (MCP) stack located behind the input window. The photoelectron is thus amplified up to several million times by secondary emission from the microchannel walls. The resulting electrons exit the back of the MCP and are proximity focused onto a position-sensing anode, which is used for the determination of the x and y coordinates of the incoming photon. In the experiments described here, we used a H33D prototype (H33D Gen I) equipped with a crossed-delay line (XDL) anode.[10] A new prototype using a different technology (H33D Gen II with cross-strip or XS anode),[69] is now under test in our laboratory and will be described in future publications.

In the XDL anode H33D Gen I detector, photon localization in each spatial direction is achieved by measuring the time delay between arrival of the charges at both ends of the corresponding delay line using a time-to-digital converter (TDC) as shown in Fig. 3. The current XDL H33D detector uses a dual-channel TDC (model DSTDC-F, Sensor Sciences, Pleasant Hill, CA). Each photon's arrival time is determined separately using two different devices. First, coarse timing information (macrotime T) is associated with each position by reading out the value of a clock counter (40 MHz or 25 ns resolution) generated by a field-programmable gate array (FPGA) processing the output of the dual TDC unit. Second, precise timing information (nanotime τ) is obtained by measuring the time separating the MCP output pulse and the next laser pulse using a separate TDC (same model as above). Both sets of information (x, y, T and τ) are then associated together, provided they were acquired within a specified timeout window (~2 μs), giving three-dimensional coordinates for each photon (two spatial and one temporal, the latter being comprised of the two components T and τ).

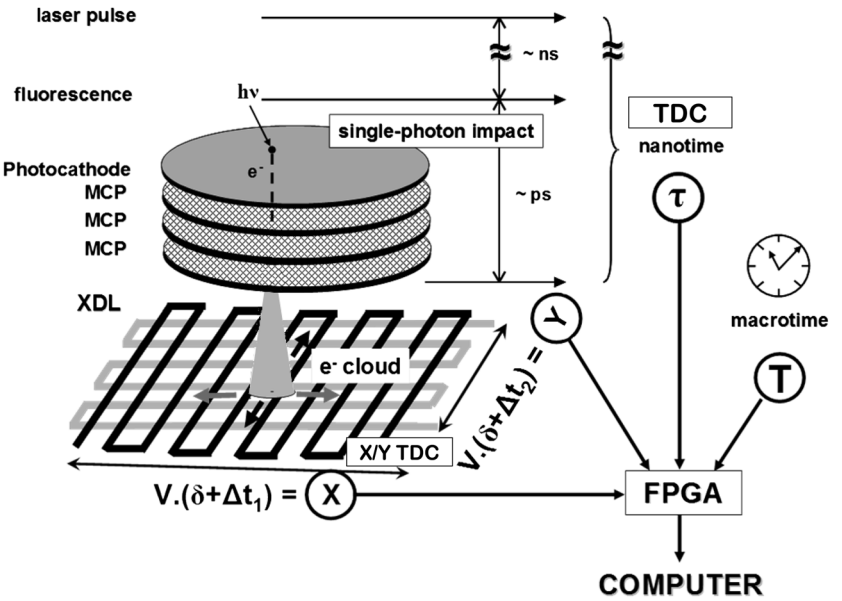

Fig. 3 Principle of the H33D detector. Each photon is converted by the photocathode into a photoelectron amplified ~10^7 times by the 3-MCP stack. The time interval between the pulse generated at the back of the MCP and the laser pulse (nanotime τ) is measured by a TDC. The electron cloud is collected by a cross-delay line anode and a timing electronics module converts the differences in charge arrival time at both ends of the delay lines into position information (X, Y). A laser pulse counter built into the readout electronics provides a 4th coordinate, the macrotime T, which is associated with the three other coordinates by a dedicated field-programmable gate array (FPGA), before being sent asynchronously to the computer. δ: fixed time delay. V: velocity factor proportional to the actual anode signal propagation velocity.[43] Adapted from Ref. 43.

2.4 *Phasor Analysis*

In phasor analysis of lifetime images, lifetime data (photon nanotimes) at each pixel is transformed into a coordinate pair called a phasor and a histogram of the number of pixels with identical phasor coordinates called a phasor plot, is generated (Fig. 4). As will be discussed below, the phasor plot is a two-dimensional representation of the distribution of lifetime values within the image. It is straightforward to highlight regions of an image corresponding to selected regions of the phasor plot. These regions of the image correspond to domains characterized by similar lifetimes. It is possible to quantitatively map these regions of the phasor plot to FRET efficiency values by introducing knowledge about the phasor coordinate of the donor and the amount of the background contribution as described elsewhere.[62,64] Alternatively, one can use the phasor coordinates corresponding to each pixel of an image to make a new quantitative image with pixel colors determined by a lifetime property of interest. The simplest example is a phasor ratio image that colors the image according to the fractional contributions two probes contribute to the signal at each pixel as described below.

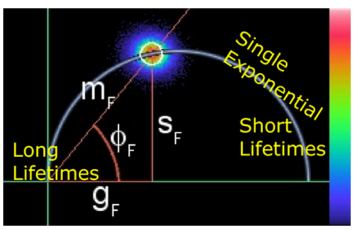

Fig. 4 The structure of a phasor plot is shown. Single exponential lifetimes are located on the semicircle, short lifetimes are located near the bottom right intersection with the x axis, and long lifetimes are located near the origin. g_F and s_F are the vector components along the g and s axes for each phasor, while m_F and φ_F are their geometric counterparts representing the modulation and phase of each phasor. The data shown is for a bulk measurement of fluorescein.[20]

First we consider the ideal case of a delta function IRF. A phasor coordinate (g, s) is calculated using a simple average of cosine and sine of the nanotimes,[58]

$$g = \frac{1}{N}\sum_{i=1}^{N} \cos(2\pi\tau_i/P), \tag{7}$$

$$s = \frac{1}{N}\sum_{i=1}^{N} \sin(2\pi\tau_i/P), \tag{8}$$

where the τ_i's are the nanotime values of all photons, $P = 1/f$ is the phasor period and N is the number of photons. The phasor frequency f will be used in the following and is usually taken as an integer multiple of the laser repetition frequency (e.g. 19 MHz = 4.75 MHz $*$ 4 for the data in Figs. 8 and 9).

By extension, one can define the fundamental phasor coordinate of a photon with nanotime τ as:

$$g = \cos(2\pi f\tau), \tag{9}$$

$$s = \sin(2\pi f\tau), \tag{10}$$

In other words, the nanotime value τ of each photon corresponds, by a simple algebraic transformation, to a fundamental phasor located on the unit circle. The average phasor value corresponding to N photons is located inside the unit disk as shown in Fig. 5. Species with a single lifetime τ have phasor coordinates centered around[58]:

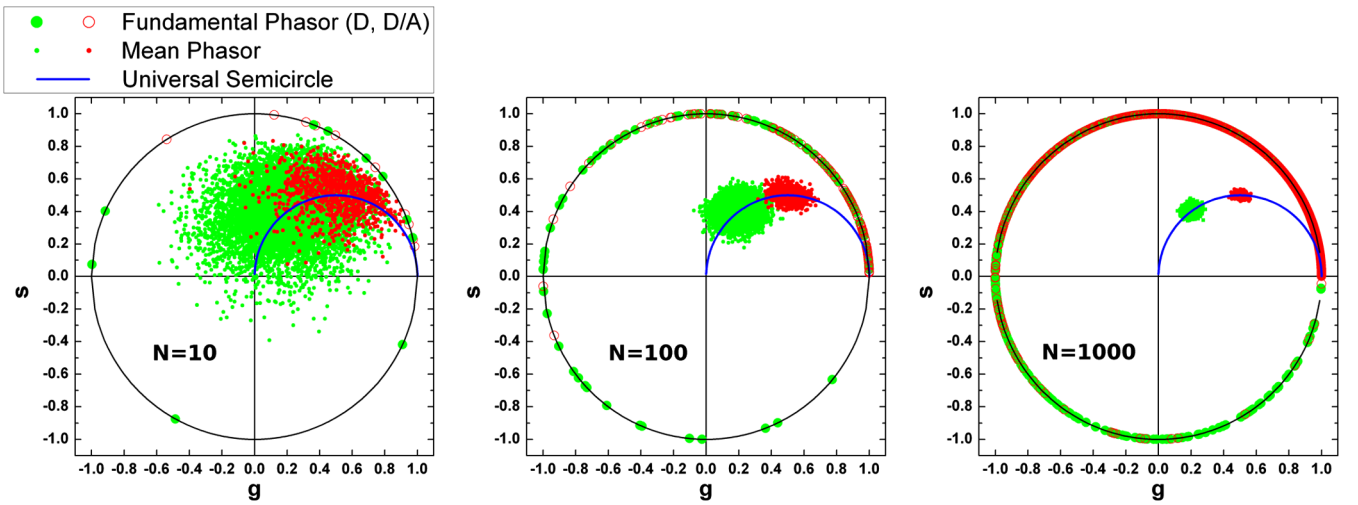

Fig. 5 Location of the fundamental phasor values and average phasor values corresponding to simulated photons emitted by a species with lifetime $\tau = 4.6$ ns (green, closer to the origin), and $\tau = 2.3$ ns (red), and using $f = 68$ MHz. For a FRET donor with a 4.6 ns lifetime, these would correspond to FRET efficiencies of 0 and 0.5. Fundamental phasor values (open circles) are located on the unit circle, which corresponds to a delta function IRF. Average values (points) of $N = 10$, 100, or 1000 are located inside the disk, but more precisely, as illustrated by 1000 simulations of such averages, close to the universal semicircle (blue) of radius 0.5 and center (0.5, 0). In each example, a single series of N fundamental phasors (open circles) is shown. The standard deviation of average phasor values around the theoretical value of Eqs. (11) and (12) varies as $N^{-1/2}$.

$$g = \frac{1}{1 + (2\pi f\tau)^2}, \tag{11}$$

$$s = \frac{2\pi f\tau}{1 + (2\pi f\tau)^2}, \tag{12}$$

that is located on the universal semicircle shown in Fig. 5. Measured phasors then appear in a statistical distribution around this center value, where for Poisson-distributed photon counts the distance from this exact location depends linearly on $N^{-1/2}$ where N is the number of photons used for the phasor average (Fig. 5).[20] Short lifetimes are located close to (1, 0) and long lifetimes located close to (0, 0) (Fig. 4). As a convenient reference, the midpoint $(1/2, 1/2)$ corresponds to a lifetime $\tau = P/2\pi$. Inverting Eqs. (11) and (12), one obtains:

$$\tau = \frac{1}{2\pi f}\left(\frac{s}{g}\right). \tag{13}$$

Species with fluorescence decays described by multiple exponentials τ_i, with relative weights f_i can be shown to have phasor coordinates:

$$g = \sum_i f_i g_i, \tag{14}$$

$$s = \sum_i f_i s_i, \tag{15}$$

$$\sum_i f_i = 1, \tag{16}$$

where the (g_i, s_i) and τ_i of each species are related by Eqs. (11)–(13). In other words, phasors add linearly and as a result, combinations of two lifetime components fall on a straight line between the two components, as shown in Fig. 6, with the position along that line determined by the relative weights of each component. The linear additivity of phasors makes this approach a powerful tool for the analysis of lifetime images comprised of multiple species as described below.

The ideal situation described above is not fundamentally modified by the existence of a finite size IRF. The IRF is accounted for by simple algebra on the phase φ and modulation m of the phasor defined by:

$$\varphi = \tan^{-1}\left(\frac{s}{g}\right), \tag{17}$$

$$m = \sqrt{g^2 + s^2}. \tag{18}$$

In the presence of an IRF, the measured and the "real" (expected) values of the phasor phase and modulation are related by:

$$\varphi_{\text{measured}} = \varphi_{\text{real}} + \varphi_{\text{IRF}}, \tag{19}$$

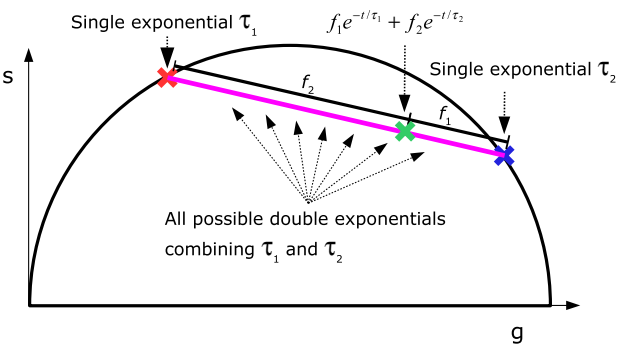

Fig. 6 The linear combination of lifetimes on the phasor plot is demonstrated using the example of adding two single-exponential phasors.

$$m_{\text{measured}} = m_{\text{real}} m_{\text{IRF}}. \tag{20}$$

Therefore, knowledge of φ_{IRF} and m_{IRF} is sufficient to recover the real phasor. φ_{IRF} and m_{IRF} can be obtained by a direct measurement of the IRF or with a measurement of a sample with a known lifetime. Note that Eqs. (19) and (20) correspond to a simple rotation and scaling of the measured data.

This simple geometric approach to handling the IRF is a particular strength of phasor analysis for both data analysis and instrument design. In contrast to the complexities of iterative deconvolution used in fitting, phasor analysis performs the deconvolution operation only once and with simple algebra, resulting in a very rapid calculation of FLIM images. For fitting by iterative deconvolution, there is a stricter requirement that the IRF be narrow and that the reference measurement be of the IRF itself. In phasor analysis, this can be done either by measuring the IRF directly (e.g., with Raman scattering or using a fluorophore with a very short lifetime), or by measuring any fluorophore with a well-known lifetime and using Eqs. (19) and (20). This also implies that maintaining an extremely narrow IRF is not necessary under phasor analysis,[20] which allows the design of hardware that optimizes other parameters such as throughput.

2.5 *Phasor Ratio Images*

The phasor plot corresponding to the lifetime information of an image can be used in different ways. The simplest way consists of selecting a region of interest (ROI) on the phasor plot and highlighting the pixels of the image with phasor values falling within this ROI. Alternatively, a color-coded phasor map can be built in order to visualize the location of all phasor values in the image. This approach is not convenient, as phasor values are themselves located in a two-dimensional space. However, in the particular case where the sample is known to contain two main species characterized by different phasor values (e.g. a short lifetime species and a long lifetime species), a phasor ratio can be computed for each pixel, which corresponds to the relative contributions of the two components, (g_0, s_0) and (g_1, s_1).[†] The phasor ratio of each pixel is computed as described in Fig. 7.

The special case for biexponential samples using a global fit considering spatial proximity to extract a ratio value for each coordinate was described previously.[64] We use a more general approach, suitable for samples with any number of decay components that utilizes spatial neighbor information by binning counts as described in Sec. 4.1 and then uses simple geometry on the phasor plot to calculate the phasor ratio.

First, the phasor is projected onto the line connecting the phasor values of the two components. The phasor ratio is then obtained as the relative distance of this projection from the first component (a phasor value projected onto the first component's phasor has a phasor ratio of zero, while a phasor value projected onto the second component's phasor has a phasor ratio of one) defining:

[†]Note that the two species do not need to be characterized by a single fluorescence lifetime. What matters is that they each can be identified by a single phasor value.

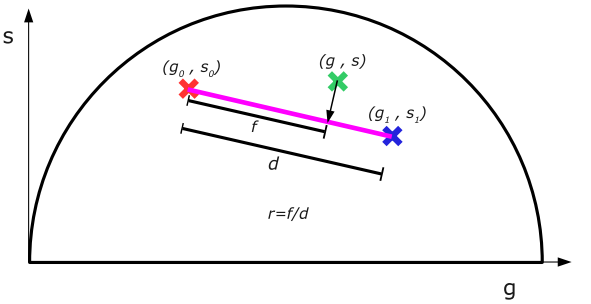

Fig. 7 This schematic shows the geometric projection which is performed to determine the phasor ratio of a point (g, s), showing the relative contributions of two known components: (g_0, s_0) and (g_1, s_1).

$$\theta = \tan^{-1}\left(\frac{s_1 - s_0}{g_1 - g_0}\right), \tag{21}$$

$$d = \sqrt{(s_1 - s_0)^2 + (g_1 - g_0)^2}, \tag{22}$$

the phasor ratio for each pixel with phasor (g, s) is given by

$$r = \frac{(g - g_0)\cos\theta + (s - s_0)\sin\theta}{d} = \frac{f}{d}, \tag{23}$$

where f/d is shown in Fig. 7. The phasor ratio can then be easily color-coded from 0 to 1 and represented for each pixel of the image. The resulting phasor-ratio map displays the relative contributions of the two known species characterized by two distinct phasor values, as in the case of two fluorescent species with different lifetimes or two populations of a FRET construct with different FRET states.

2.6 *Data Acquisition and Analysis*

Data acquired by the H33D detector was analyzed using custom software (IdefiX) developed using LabVIEW (National Instruments, Austin, TX) and C/C++ (Visual Studio 6.0, Microsoft Corp., Seattle; gcc/g++ 4.x, GNU/FSF, Boston). This software permits live data display and analysis during acquisition and postprocessing of saved raw data.

Typically, since the H33D detector generates a photon stream consisting of (x, y, τ, T) values, the first task consists of binning this stream temporally based on the macrotime T of each photon, thus defining "frames." The second step consists of the formation of an intensity image corresponding to each frame. Since each coordinate x or y is encoded in 12 bits, the image consists of at most 4096×4096 "pixels." However, the effective spatial resolution for photons striking the 25 mm surface of the photocathode in the detector is about 50 to 100 μm, which results in around 250 to 500 effective pixels in each direction. Therefore, a spatial binning factor of 8 to 16 is typically used in order to obtain 512×512 to 256×256 pixel images with better contrast. The intensity value at each pixel is determined from the number of photons having these spatial coordinates within a given frame time. The software allows defining regions of interest (ROI) in the image, and it computes intensity time traces as well as nanotime histograms for each ROI.

In addition to representing the raw data of the H33D detector, the software computes a phasor for each photon. Using

Eqs. (9) and (10), the nanotime value τ for each single photon is associated with a single-photon phasor coordinate (g_τ, s_τ) called a fundamental phasor. Because phasors add linearly, these fundamental phasors can be added within each pixel to form G- and S-phasor "images." Normalization by the intensity image, which is nothing but the map of N values in Eqs. (7) and (8), provides the g and s phasor values for each pixel. This procedure allows extremely rapid generation as well as simple storage of phasor data. The previous sections have described how to obtain phasor plots and phasor ratio images from this data.

3 Results

3.1 *Phasor-Ratio Imaging of Live EGFP-Expressing and Quantum Dot-Labeled Cells*

To demonstrate the capabilities of phasor analysis with the H33D, we analyzed live-cell imaging data acquired with the H33D. HeLa cells expressing caveolin 1-EGFP and glycosyl-phosphatidylinositol (GPI)-anchored avidin were labeled with nonbiotinylated quantum dots emitting at 620 nm and observed using epifluorescence microscopy.[33]

Figs. 8(a)–8(c) shows the distribution of the two probes in the sample illustrated by spectral separation of each probe's emission using distinct emission filters (same excitation at 442 nm). Figure 8(a) shows the EGFP signal revealing the distribution of caveolin, while Fig. 8(b) shows the quantum dot signal, which appears to be largely concentrated near the nuclei. In Fig. 8(c), the overlay of these two signals is shown.

The data for Fig. 8(d)–8(f) was acquired on the same sample, but using a long pass filter (500LP), which allowed us to detect the total emission of EGFP, autofluorescence, and quantum dots. Figure 8(d) shows the integrated intensity, where it is no longer possible to clearly distinguish the EGFP and quantum dot regions. In Fig. 8(e), the phasor coordinates for EGFP ($g = 0.58$, $s = 0.35$) and quantum dots ($g = 0.28$, $s = 0.41$) are used to define a phasor ratio image [Fig. 8(f)] in which the green color corresponds to a complex multiexponential phasor formed by EGFP combined with cell autofluorescence, while the red color corresponds to a multiexponential phasor given by the quantum dots. With this representation, it is easy to see the contrast between regions that are dominated by EGFP and regions that are dominated by quantum dot fluorescence. In particular, one recovers the membrane localization of the EGFP signal and the perinuclear localization of quantum dots observed in the spectrally separated images of Fig. 8(c). In contrast, attempts to obtain a lifetime image map by fitting to this dataset were unsuccessful[43] due to the small number of counts (tens of thousands for QDs, thousands or less for GFP), the count disparity, and the highly multiexponential nature of the QD, GFP, and autofluorescence lifetimes. Thus phasor analysis yielded a straightforward result in a complicated sample that we could not analyze with conventional fitting approaches.

The same principle of operation demonstrated by this dataset could also be used with a FRET construct to display the ratio between binary FRET states, or with slight modification, to color an image based on a FRET value. These algorithms are also sufficiently rapid that they can be used to display a phasor ratio image and phasor plot during live acquisition. A simple illustration of this capability was provided in Ref. 32.

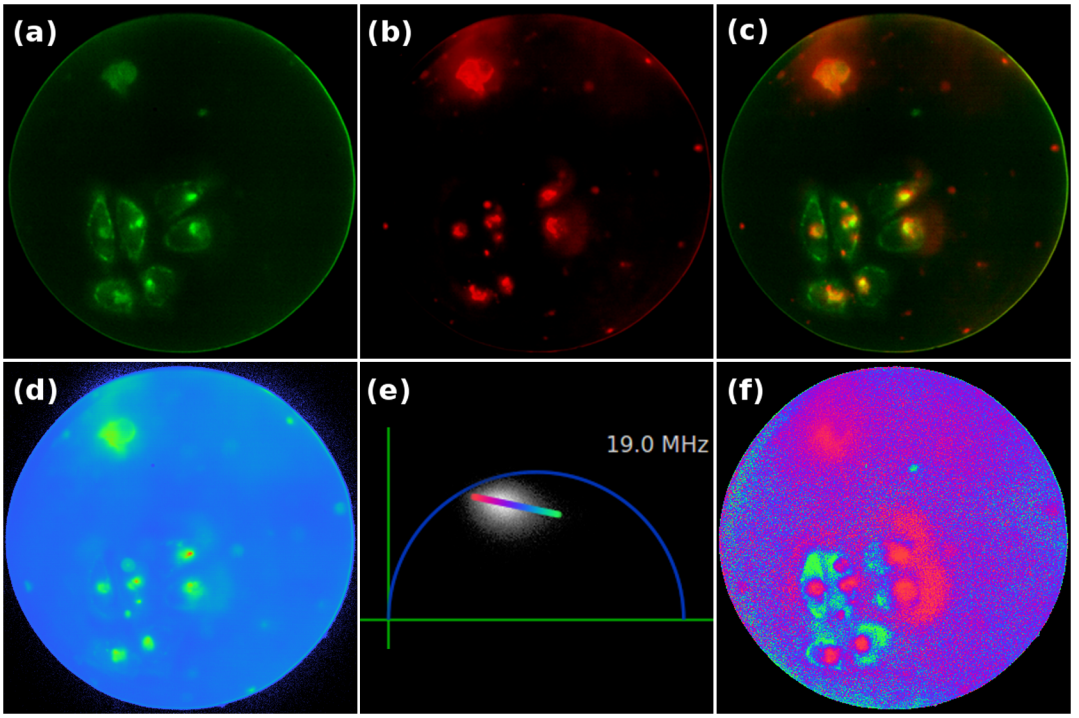

Fig. 8 H33D data of HeLa cells expressing caveolin 1-EGFP and GPI-anchored avidin labeled with biotinylated quantum dots emitting at 620 nm. (a)–(c) are adapted from Ref. 43 and are using different emission filters: (a) 530DF30, (b) 615DF45, (c) 530DF30 as green overlapped with 615DF45 as red; (d)–(f) are with a 500LP filter which collected both emitters; (d) shows an intensity image, (e) shows the phasor plot with a color bar showing the phasor ratio coloring, and (f) shows a phasor ratio plot with hue values determined according to the projection in (e).

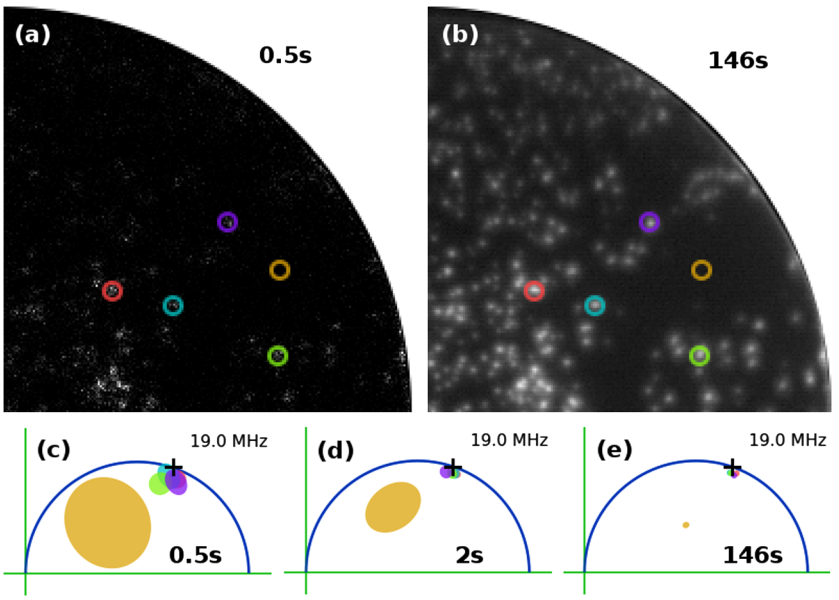

Fig. 9 H33D data of fluorescent Nile Red beads at various frame durations, with approximately 150 counts per second per bead. (a), (b) From one quadrant of the H33D detector, four ROIs containing beads are shown (red, blue, green, purple), and one ROI containing background (orange). (c)–(e) For each ROI the center of mass phasor coordinates are shown as ellipses corresponding to one standard deviation of phasor uncertainty along the phase and modulation axes. The cross (+) shows the center lifetime value for these beads of 6 ns.

3.2 *Single-bead Imaging and Frame Rates*

The application of phasor analysis to point sources was demonstrated with measurements of 220 nm diameter beads shown in Fig. 9. We selected ROIs corresponding to bead positions [Figs. 9(a) and 9(b)], and computed the center of mass of the phasors within each spatial ROI. Then, we used the analytical expressions for phasor uncertainty in phase and modulation[20] to define the size of an ellipse (1σ radially) to plot an ellipse (semi-axes: sigma_phi, sigma_m as defined in Ref. 20), which represents the phasor coordinate for each bead and its precision [Figs. 9(c)–9(e)]. Approximately 150 cps/bead were observed. We have measured the lifetime of these beads to be 6 ns, and in each of Figs. 9(c)–9(e) the phasor coordinate corresponding to 6 ns is marked with a cross to illustrate the deviation of individual bead measurements from the correct value. In Fig. 9(c), the phasor precision for a 0.5 s frame is shown as sufficient to distinguish phasors at a separation larger than the ellipse size. This shows the capability for subsecond frame rates, constrained only by the count rate obtainable for each particle. When rebinned to 2 s frames as shown in Fig. 9(d), the precision doubles as expected.

After identifying the region of the phasor plot corresponding to a probe of interest, one can isolate that probe in future measurements without performing any intensity thresholding. For example, if one has a single measurement containing both beads and quantum dots, then by selecting a region of interest on the phasor plot corresponding to the location of their phasors, one can highlight only the pixels of the image containing beads with those lifetimes. With this approach, it should be possible to efficiently track point sources using a purely phasor-based contrast and exploit this information to extract information on the probe's dynamic behavior. Alternatively, one can track point sources by intensity, and observe the dynamics of lifetime changes in the phasor plot.

4. Discussion and Conclusion

4.1 *Combination of Widefield Single-Photon Counting and Phasor Analysis*

We have demonstrated the combination of phasor analysis and the generation of phasor ratio images with the widefield single-photon counting H33D Gen I detector. We have shown that this approach provides a simple and rapid way to generate fluorescence lifetime maps with easy-to-interpret lifetime information (phasor ratio maps). The speed of phasor calculation makes it possible in principle to display live phasor movies during data acquisition. Moreover, the additivity of phasors allows to arbitrarily rebin the stream of photons, yielding a lifetime image sequence optimizing the SNR or with any desired frame rate. Indeed, the precision of each phasor coordinate increases with the square root of the number of counts. Since the H33D detector provides a raw stream of photon counts, the phasor values can be binned with different spatial resolution and temporal resolution (frame rate) to obtain the average number of photons per pixel needed for a particular phasor precision. The flexible nature of the H33D data stream also means that data from a single acquisition can be examined with different spatial, temporal, or lifetime resolution.

Since roughly 100 photons are required to clearly separate, for instance, a FRET pair efficiency of 0 from one of 0.5 in the phasor plot (Fig. 5), and since the maximum local count rate of the H33D Gen I detector is ~10 kHz, integration times as short as 10 ms should be sufficient to build a FLIM map which distinguishes several species by fluorescence lifetime contrast only. As discussed in Sec. 1.4.1, this is only possible for sparsely labeled samples (low f value), due to the global count rate limitation of the H33D Gen I prototype. This could allow high spatial and temporal resolution tracking of single-molecules

with lifetime contrast, giving access to information on each single-molecule's environment.

4.2 *Future Development*

Our H33D Gen I prototype is constrained to a maximum global count rate of ~500 kHz due to electronic limitations and a local count rate of ~10 kHz due to MCP saturation. A new generation of H33D detector comprising a number of improvements was recently developed and is currently being tested. Use of a different position-sensing anode (cross-strip or XS anode)[68] allows a reduction of the MCP gain while preserving the spatial resolution of the detector. This MCP gain reduction allows increasing the maximum local count rate to ~100 kHz. As argued previously, this could permit sparsely-labeled millisecond-range FLIM movie rates within the detector's global count rate limitation.

The H33D Gen I prototype's maximum global count rate limitation is primarily set by the dead time of the TDC units used for positioning and nanotime determination. This restriction is significantly relaxed by using a XS anode, which does not use a TDC for position readout. The H33D Gen II has achieved an order of magnitude larger global readout rate (several MHz). Using one (or more) TDCs to extract nanotime information for each photon would re-introduce a strong count rate limitation due to TDC deadtime. Although the XS anode does not provide the precision of photon timing obtained with a TDC (the timing resolution of each event is of the order of 1–2 ns),[69] it should be sufficient to perform phasor analysis of lifetime with high precision because phasor analysis does not require as good of a timing precision for precise lifetime analysis compared to exponential fitting.[20]

The H33D Gen II prototype also improves on the quantum efficiency of the first generation, reaching a $QE \sim 15\%$ in the visible range of the spectrum. This will allow fainter and redder samples to be observed more efficiently and with better contrast, eventually reaching single organic fluorophore sensitivity.

4.3 *Conclusion*

We have shown that the combination of a widefield single-photon counting detector such as the H33D detector and phasor analysis has numerous advantages over more conventional raster-scanning and fluorescence decay fitting approaches in terms of acquisition speed, required excitation power, computational simplicity, and ease of interpretation. We have illustrated its application to live-cell imaging and single fluorophore (quantum dot) detection. Many more applications could benefit from a similar approach and from detectors with better sensitivity and larger global count rates.

Acknowledgments

This work was supported by the grants NIH-BRG 5R01EB006353, NSF-IDBR 0552099, and NIH EB000312-06A2. We thank Fabien Pinaud and Gopal Iyer for assistance with sample preparation.

References

1. X. Michalet et al., "The Power and Prospects of Fluorescence Microscopies and Spectroscopies," *Annu. Rev. Biophys. Biomol. Struct.* **32**(1), 161–182 (2003).
2. X. F. Wang et al., "Fluorescence lifetime imaging microscopy (FLIM)—instrumentation and applications," *Crit. Rev. Anal. Chem.* **23**(5), 369–395 (1992).
3. J. R. Lakowicz et al., "Fluorescence lifetime imaging," *Anal. Biochem.* **202**(2), 316–330 (1992).
4. T. W. J. Gadella, Jr, T. M. Jovin, and R. M. Clegg, "Fluorescence lifetime imaging microscopy (FLIM): spatial resolution of microstructures on the nanosecond time scale," *Biophys. Chem.* **48**(2), 221–239 (1993).
5. R. M. Clegg, "Fluorescence imaging spectroscopy and microscopy," John Wiley & Sons, Hoboken, NJ (1996).
6. K. Suhling, P. M. W. French, and D. Phillips, "Time-resolved fluorescence microscopy," *Photochem. Photobiol. Sci.* **4**(1), 13–22 (2005).
7. K. Suhling, "Fluorescence lifetime imaging," in *Cell Imaging*, D. Stephens, Ed., Scion Publishing, Bloxham, UK (2006).
8. J. A. Levitt et al., "Fluorescence lifetime and polarization-resolved imaging in cell biology," *Curr. Opin. Biotechnol.* **20**(1), 28–36 (2009).
9. M. Dahan et al., "Time-gated biological imaging by use of colloidal quantum dots," *Opt. Lett.* **26**(11), 825–827 (2001).
10. X. Michalet et al., "Photon-counting H33D detector for biological fluorescence imaging," *Nucl. Instrum. & Meth. A* **567**, 133–136 (2006).
11. R. Sanders et al., "Quantitative pH imaging in cells using confocal fluorescence lifetime imaging microscopy," *Anal. Biochem.* **227**(2), 302–308 (1995).
12. J. R. Lakowicz, H. Szmacinski, and M. L. Johnson, "Calcium imaging using fluorescence lifetimes and long-wavelength probes," *J. Fluoresc.* **2**(1), 47–62 (1992).
13. J. R. Lakowicz et al., "Fluorescence lifetime imaging of calcium using Quin-2," *Cell Calcium* **13**(3), 131–147 (1992).
14. H. Szmacinski and J. R. Lakowicz, "Sodium green as a potential probe for intracellular sodium imaging based on fluorescence lifetime," *Anal. Biochem.* **250**(2), 131–138 (1997).
15. A. V. Agronskaia, L. Tertoolen, and H. C. Gerritsen, "Fast fluorescence lifetime imaging of calcium in living cells," *J. Biomed. Opt.* **9**, 1230 (2004).
16. K. M. Hanson et al., "Two-photon fluorescence lifetime imaging of the skin stratum corneum pH gradient," *Biophys. J.* **83**(3), 1682–1690 (2002).
17. Y. Chen, J. D. Mills, and A. Periasamy, "Protein localization in living cells and tissues using FRET and FLIM," *Differentiation* **71**(9–10), 528–541] (2003).
18. R. D. Spencer and G. Weber, "Measurements of subnanosecond fluorescence lifetimes with a cross-correlation phase fluorometer," *Ann. N. Y. Acad. Sci.* **158**(1), (1969).
19. H. C. Gerritsen et al., "Fluorescence lifetime imaging in scanning microscopy," in *Handbook of Biological Confocal Microscopy*, J. B. Pawley, Ed., pp. 516–534, Springer, New York, NY (2006).
20. R. A. Colyer, C. Lee, and E. Gratton, "A novel fluorescence lifetime imaging system that optimizes photon efficiency," *Microsc. Res. Tech.* **71**(3), 201–213 (2008).
21. W. Becker, "Advanced time-correlated single photon couting techniques," in *Chemical Physics*, A. W. J. Castleman, J. P. Toennies, and W. Zinth, Eds., Springer, Berlin (2005).
22. N. Callamaras and I. Parker, "Construction of a confocal microscope for real-time $x-y$ and $x-z$ imaging," *Cell Calcium* **26**(6), 271–279 (1999).
23. X. F. Wang et al., "A two-dimensional fluorescence lifetime imaging system using a gated image intensifier," *Appl. Spectrosc.* **45**(3), 360–366 (1991).
24. K. Dowling et al., "2-D fluorescence lifetime imaging using a time-gated image intensifier," *Opt. Commun.* **135**(1–3), 27–31 (1997).
25. J. Requejo-Isidro et al., "High-speed widefield time-gated endoscopic fluorescence-lifetimeimaging," *Opt. Lett.* **29**(19), 2249–2251 (2004).
26. C. Buranachai et al., "Rapid frequency-domain FLIM spinning disk confocal microscope: lifetime resolution, image improvement and wavelet analysis," *J. Fluoresc.* **18**(5), 929–942 (2008).
27. E. B. van Munster et al., "Combination of a spinning disc confocal unit with frequency-domain fluorescence lifetime imaging microscopy," *Cytometry* **71A**(4), 207–214 (2007).
28. D. M. Grant et al., "Optically sectioned fluorescence lifetime imaging using a Nipkow disk microscope and a tunable ultrafast continuum excitation source," *Opt. Lett.* **30**(24), 3353–3355 (2005).

29. K. C. B. Lee et al., "Application of the Stretched Exponential Function to Fluorescence Lifetime Imaging," *Biophys. J.* **81**(3), 1265–1274 (2001).
30. A. A. Istratov and O. F. Vyvenko, "Exponential analysis in physical phenomena," *Rev. Sci. Instrum.* **70**(2), 1233–1257 (1999).
31. R. R. Duncan et al., "Multidimensional time-correlated single photon counting (TCSPC) fluorescence lifetime imaging microscopy (FLIM) to detect FRET in cells," *J. Microsc.* **215**(1), 1–12 (2004).
32. X. Michalet et al., "Single-quantum dot imaging with a photon counting camera," *Curr. Pharm. Biotechnol.* **10**(5), 543–558 (2009).
33. X. Michalet et al., "A space- and time-resolved single-photon counting detector for fluorescence microscopy and spectroscopy," *SPIE Proc.* **6092**, 60920M (2006).
34. J. A. Spitz et al., "Scanning-less wide-field single-photon counting device for fluorescence intensity, lifetime and time-resolved anisotropy imaging microscopy," *J. Microsc.* **229**(1), 104–114 (2008).
35. S. Shrestha et al., "High-speed multispectral fluorescence lifetime imaging implementation for in vivo applications," *Opt. Lett.* **35**(15), 2558–2560 (2010).
36. C. G. Hübner et al., "Single-molecule fluorescence—Each photon counts, in single molecule spectroscopy," R. Rigler, M. Orrit, and T. Basche, Eds., Springer, Verlag, Stockholm (2001).
37. L. A. Kelly et al., "Simultaneous resolution of spectral and temporal properties of UV and visible fluorescence using single-photon counting with a position-sensitive detector," *Rev. Sci. Instr.* **66**(2), 1496–1498 (1995).
38. L. A. Kelly, J. G. Trunk, and J. C. Sutherland, "Time-resolved fluorescence polarization measurements for entire emission spectra with a resistive-anode, single-photon-counting detector: the fluorescence omnilyzer," *Rev. Sci. Instr.* **68**(6), 2279–2286 (1997).
39. K. Kemnitz et al., "Fluorescence lifetime imaging of cells on the picosecond timescale," *Proc. SPIE* **2926**, 177–187 (1996).
40. K. Kemnitz, L. Pfeifer, and M. R. Ainbund, "Detector for multichannel spectroscopy and fluorescence lifetime imaging on the picosecond timescale," *Nucl. Instr. Meth. Phys. Res.* **387**, 86–87 (1997).
41. M. Tramier et al., "Picosecond-Hetero-FRET microscopy to probe protein-protein interactions in live cells," *Biophys. J.* **83**(6), 3570–3577 (2002).
42. V. Emiliani et al., "Low-intensity two-dimensional imaging of fluorescence lifetimes in living cells," *Appl. Phys. Lett.* **83**(12), 2471–2473 (2003).
43. X. Michalet et al., "Fluorescence lifetime microscopy with a time- and space-resolved single-photon counting detector," *Proc. SPIE* **6372**, 63720E (2006).
44. X. Michalet et al., "Detectors for single-molecule fluorescence imaging and spectroscopy," *J. Mod. Opt.* **54**, 239–282 (2007).
45. R. A. Colyer et al., "Phasor-based single-molecule fluorescence lifetime imaging using a wide-field photon-counting detector," *Proc. SPIE* **7185** (0T), 1–10 (2009).
46. O. H. W. Siegmund et al., "Microchannel plate imaging photon counters for ultraviolet through NIR detection with high time resolution," *Proc. SPIE* **8033**, 80330V (2011).
47. M. Köllner and J. Wolfrum, "How many photons are necessary for fluorescence-lifetime measurements," *Chem. Phys. Lett.* **200**(1–2), 199–204 (1992).
48. E. G. Novikov et al., "Linear algorithms for stretched exponential decay analysis," *Opt. Commun.* **166**(1–6), 189–198 (1999).
49. H. P. Good, A. J. Kallir, and U. P. Wild, "Comparison of fluorescent lifetime fitting techniques," *J. Phys. Chem.* **88**(22), 5435–5441 (1984).
50. S. Pelet et al., "A fast global fitting algorithm for fluorescence lifetime imaging microscopy based on image segmentation," *Biophys. J.* **87**(4),2807–2817 (2004).
51. M. Maus et al., "An experimental comparison of the maximum likelihood estimation and nonlinear least-squares fluorescence lifetime analysis of single molecules," *Anal. Chem.* **73**(9), 2078–2086 (2001).
52. W. Becker et al., "Fluorescence lifetime imaging by time-correlated single-photon counting," *Microsc. Res. Tech.* **63**(1), 58–66 (2004).
53. G. H. Patterson and D. W. Piston, "Photobleaching in two-photon excitation microscopy," *Biophys. J.* **78**(4), 2159–2162 (2000).
54. J. Enderlein and R. Erdmann, "Fast fitting of multiexponential decay curves," *Opt. Commun.* **134**(1–6), 371–378 (1997).
55. S. Andersson-Engels, J. Johansson, and S. Svanberg, "The use of time-resolved fluorescence for diagnosis of atherosclerotic plaque and malignant tumours," *Spectrochimica Acta Part A: Mol. Spectrosc.* **46**(8), 1203–1210 (1990).
56. J. R. Lakowicz et al., "Analysis of fluorescence decay kinetics from variable-frequency phase shift and modulation data," *Biophys. J.* **46**(4), 463–477 (1984).
57. Y.-C. Chen and R. Clegg, "Fluorescence lifetime-resolved imaging," *Photosynth. Res.* **102**(2), 143–155 (2009).
58. D. M. Jameson, E. Gratton, and R. D. Hall, "The measurement and analysis of heterogeneous emissions by multifrequency phase and modulation fluorometry," *Appl. Spectrosc. Rev.* **20**(1), 55–106 (1984).
59. P. J. Verveer, A. Squire, and P. I. H. Bastiaens, "Global analysis of fluorescence lifetime imaging microscopy data," *Biophys. J.* **78**(4), 2127–2137 (2000).
60. A. H. A. Clayton, Q. S. Hanley, and P. J. Verveer, "Graphical representation and multicomponent analysis of single-frequency fluorescence lifetime imaging microscopy data," *J. Microsc.* **213**(1), 1–5 (2004).
61. G. I. Redford and R. M. Clegg, "Polar plot representation for frequency-domain analysis of fluorescence lifetimes," *J. Fluoresc.* **15**(5), 805–815 (2005).
62. M. A. Digman et al., "The phasor approach to fluorescence lifetime imaging analysis," *Biophys. J.* **94**(2), L14–L16 (2008).
63. A. H. A. Clayton, "The polarized AB plot for the frequency-domain analysis and representation of fluorophore rotation and resonance energy homotransfer," *J. Microsc.* **232**(2), 306–312 (2008).
64. H. E. Grecco, P. Roda-Navarro, and P. J. Verveer, "Global analysis of time correlated single photon counting FRET-FLIM data," *Opt. Exp.* **17** (8), 6493–6508 (2009).
65. S. Schlachter et al., "mhFLIM: resolution of heterogeneous fluorescence decays in widefield lifetime microscopy," *Opt. Exp.* **17**(3), 1557–1570 (2009).
66. F. Pinaud et al., "Bioactivation and cell targeting of semiconductor CdSe/ZnS nanocrystals with phytochelatin-related peptides," *J. Am. Chem. Soc.* **126**(19), 6115–6123 (2004).
67. F. Pinaud et al., "Dynamic partitioning of a glycosyl-phosphatidylinositol-anchored protein in glycosphingolipid-rich microdomains imaged by single-quantum dot tracking," *Traffic* **10**(6), 691–712 (2009).
68. O. H. W. Siegmund et al., "Cross delay line detectors for high time resolution astronomical polarimetry and biological fluorescence imaging," *IEEE Nucl. Sci. Symp. Conf. Rec. N14-55*, 448–452 (2005).
69. A. S. Tremsin et al., "High speed multichannel charge sensitive data acquisition system with self-triggered event timing," *IEEE Nucl. Sci. Symp. Conf. Rec.* **56**(3), 1148–1152 (2009).